

# HIGH EFFICIENCY DIODE PUMPED Nd:YAG LASERS BASED ON A CERAMIC SLAB ACTIVE MEDIUM

*Antonio Lapucci and Marco Ciofini*

Istituto Nazionale di Ottica (C.N.R.), Largo Enrico Fermi 6, 50125 Firenze, Italy

## 1. Introduction

High power semiconductor diode-laser bars have experienced a tremendous development over the past 15-20 years. Higher levels of per-element output powers as well as higher power conversion efficiencies have been achieved. Today, industrial grade diode lasers are exceeding 120 W Continuous Wave (CW) from a standard 10 mm bar. QCW (Quasi-Continuous Wave) devices at 808 nm already exceed 300 W per bar. The efficiency of state of the art diode-laser materials has passed the 60% level [1]. At the same time diode-laser bars have significantly decreased in cost, following a learning curve similar to other semiconductor manufacturing processes. Prices have passed from several hundred of dollars per Watt of the early 90s to the actual figure of less than 10 \$ / W of commercial CW stacks down to 1 \$ /W in the large QCW stacks used for inertial fusion studies [2].

This astonishing growth in laser diodes technology has resulted in a correspondingly large development of Diode Pumped Solid State Laser (DPSSL) sources. Pumping of Solid State lasers in the Rod, Disc, Slab or Fiber format is at present the largest application market of diode laser sources [3].

The different DPSSL formats present their own advantages and disadvantages. The fiber- [4] and disc-laser [5] formats have both proven extremely effective in terms of efficiency and extracted beam quality but they have a higher technological complexity along with the existence of a number of proprietary solutions. Rod schemes usually present a disadvantageous trade-off between extraction efficiency and optical quality of the extracted beam. For these reasons, from the very beginning of our research activity, our choice has been focused on a slab format [6] and all our experimental devices share the use of slabs of ceramic Nd:YAG active material [7], with direct diode pumping. Similar geometries have been adopted in some important parallel work [8]-[10].

In this chapter we will describe some results accumulated over several years of research activity, pointing out advantages and drawbacks of the slab geometry for high average power applications. In our experiments different solutions have been tested for the pumping and

cooling schemes as well as for the mode propagation inside the active material, with the aim of overcoming the problems induced by active medium thermal deformations. We have been designing and testing several different prototypes of Ceramic Slab Lasers pumped by various laser diode arrays in vertical and horizontal stacks. We have investigated most of the possible variations of the slab geometry. To reduce thermal effects, different architectures with transverse zig-zag propagation have been studied and compared. Face- and edge-pumping schemes have been adopted with the different diode stacks configurations. Finally the use of multipass-stable or hybrid stable-unstable resonators in conjunction with this particular active medium geometry has been thoroughly investigated both in CW and in Pulsed operation. Compactness, efficiency and ruggedness have been the principal design drivers of our work. Nevertheless high beam quality and insensitivity to diode temperature have also been sought.

Advantages and disadvantages of the various solutions are here described and the best achieved results of each configuration are summarized.

## 2. Zig-Zag Slab Laser Geometry

In a solid state laser, a slab format has the main advantage of reducing the deleterious effects of thermal gradients inside the active medium. A rod shaped laser has cylindrically shaped gradients that produce thermal focusing, biaxial lens effect and birefringence [11], [12]. Effects that practically limit the high power operation of rods and strongly affect the trade-off between power extraction and beam quality. This problem is differently overcome in fiber [13, 14], disc [5, 15] and slab [6, 8, 16, 17] lasers. The fiber laser maintains the cylindrical geometry but generously raises the thermal limits thanks to an extremely high aspect-ratio. Disc and slab lasers face the thermal distortion problems, “controlling” their effects. Indeed in these cases one can design optical paths in the active medium that are parallel to the thermal gradients or that visit different parts of the medium averaging the gradients effects. Moreover geometries are possible (both in the disc and in the slab cases) in which cooling and pumping directions are parallel and thus gradients are strongly reduced. For such reasons, a slab geometry with internal zig-zag propagation and direct diode pumping represents a promising design to obtain high power lasers. This configuration presents also other advantages, such as linear polarization of the laser light, absence of antireflection coatings for the laser wavelength and about 97% superposition of laser modes with the pumped volume, as will be discussed in this paragraph.

In the following the  $z$  axis is considered coincident with the laser propagation direction. The slab will be oriented with its longer dimension  $L$  along  $z$ , the width  $W$  along  $y$ , and the thickness  $T$  along  $x$ , with the general condition  $L > W > T$ . Zig-zag propagation paths in the  $x - z$  plane of the active medium can be achieved by cutting the two slab ends at the Brewster angle (Figure 1).

The Nd:YAG refractive index @  $\lambda = 1.064 \mu\text{m}$  is  $n = 1.817$ , so that

$$\theta_B = \text{atan}(n) = 61.2^\circ \quad (1)$$

and thus the slab ends have to be prepared with an edge angle

$$\alpha = 90^\circ - \theta_B = 28.8^\circ \quad (2)$$

With this choice, the zig-zag path takes place in the x-z plane, and the internal incidence angle of the laser beam on the large LxW faces is easily calculated to be

$$\gamma = 57.6^\circ. \quad (3)$$

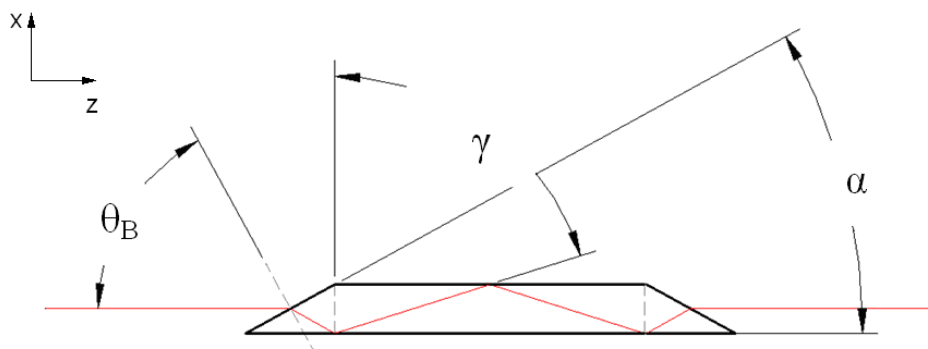


Figure 1. Geometry of the internal zig-zag propagation.

This last angle is much larger than the limit angle  $\varphi = \arcsin(1/n) = 33.4^\circ$ , so that low optical losses within the slab would be guaranteed by Total Internal Reflection (TIR). As a matter of fact, in order to prevent TIRs being frustrated by any mechanical mountings or gaskets, the large LxW faces are to be coated with a thick ( $2 \div 5 \mu\text{m}$ ) layer of  $\text{SiO}_2$  (refractive index  $n' = 1.45$ ) [10], [11]; the limit angle becomes  $\varphi' = \arcsin(n'/n) = 52.9^\circ$  still remaining below the value of the incidence angle  $\gamma$ .

The slab length should be calculated considering that the internal zig-zag path must consist of an integer number of legs. If an odd number  $2k + 1$  is chosen, the slab shape will be of the “roof” type and the slab dimensions are given by

$$L' = (2k + 1) T / \tan(90^\circ - \gamma) + T / \tan(\alpha), \quad (4)$$

$$L = L' - 2T / \tan(\alpha), \quad (5)$$

where  $T$  is the slab thickness, and  $L'$  and  $L$  are the longer and shorter sides, respectively. If an even number  $2k$  is chosen, the slab shape will be of the “parallelogram” type and the slab edge-to-edge length is

$$L = 2k T / \tan(90^\circ - \gamma). \quad (6)$$

It is also important to observe that such a geometrical scheme presents the further advantage of producing a high filling factor of the laser beam in the active medium. In fact the edge angle  $\alpha$  has a numerical value very close to the angle  $90^\circ - \gamma = 32.4^\circ$  formed by any internally travelling ray and the slab (totally) reflecting faces. It can be easily verified that a beam impinging on the Brewster window with a transverse width equal to the slab thickness  $T$  fills more than 97% of the slab volume with obvious benefits in terms of uniformity and

gain exploitation [6, 18]. If the slab end surfaces are cut perpendicular to the  $z$  axis, it is always possible to suitably tilt the laser mirrors so that the beam enters the slab at the Brewster angle, but in this case the filling factor is strongly reduced.

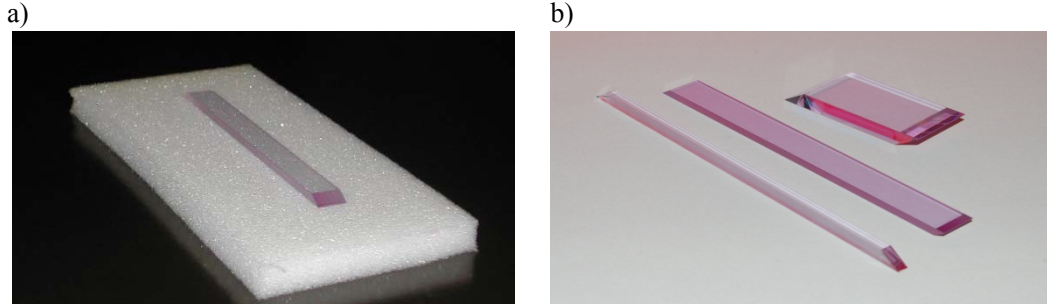


Figure 2. Images of the Ceramic Nd:YAG slabs of our experiments. a) the “roof shaped” slab described in this paragraph. b) some other samples, including the large 0.6% Nd doped “parallelogram shaped” slab described in the paragraph.

Figure 2 shows some typical Nd:YAG slabs used to build diode pumped lasers in the medium power range, that is with output power up to 1000 W. These samples consist of polycrystalline ceramic material [19-21] and are supplied by Konoshima Chemicals (Baikowski Group) [22]. Although most of the physical and optical parameters are the same as for Czochralsky-method-generated single crystals [23, 24], ceramic presents the advantages of a larger achievable doping level ( $> 4\%$ ) and a much higher fracture limit stress. As case studies, we will characterize here the slab visible in Figure 2a) and the last slab on the right side of Figure 2b). The first slab is “roof shaped” with  $W = 10$  mm,  $T = 3$  mm and  $L' = 114.2$  mm (23 internal bounces), the Nd doping being 1%. The second slab is “parallelogram shaped” with  $W = 20$  mm,  $T = 4$  mm and  $L = 37.8$  mm (6 internal bounces), the Nd doping being 0.6%.

The laser threshold condition in terms of the minimum pump power  $P_{th}$  needed to produce gain, can be estimated via a simplified formula, in the approximation of uniform pumping and uniform laser beam profile in the transverse plane [11]

$$P_{th} \cong \frac{hc\delta WT}{2\lambda\sigma\tau\eta}, \quad (7)$$

where  $h = 6.6 \cdot 10^{-34}$  Js is the Plank constant,  $c$  is the speed of light,  $\lambda = 808$  nm the pump wavelength,  $\sigma = 2.8 \cdot 10^{-23}$  m<sup>2</sup> the neodymium stimulated emission cross section,  $\tau$  the radiative lifetime; finally  $\delta = 0.20$  represents the cavity losses and  $\eta$  represents the fraction of pump power absorbed by the active medium. Considering that the main absorption line of Nd:YAG (@ 808 nm) is roughly 1 nm wide while standard diode bars present emission line-widths of about 3 nm [3, 25], an effective absorption coefficient can be roughly estimated as one third of the peak value (10 cm<sup>-1</sup> for 1% doping, 6 cm<sup>-1</sup> for 0.6% doping) [26]. Thus, for the 1% doped slab ( $\tau = 230$   $\mu$ s), in case the pump light impinges the two  $L \times W$  slab faces (face-pumping configuration), the absorption depth results 3 mm and by means of the exponential decay law  $\eta = 0.63$  may be estimated. With these values the estimated pump threshold for laser action is  $P_{th} = 181$  W. For the 0.6% doped slab ( $\tau = 250$   $\mu$ s), in case the pump light

impinges the two LxT slab faces (edge-pumping configuration), the available absorption depth is 20 mm and consequently  $\eta = 0.98$ . The corresponding threshold value is  $P_{th} = 286$  W. This calculation gives a rough evaluation of the minimum pump power needed to produce gain in our active media. A more accurate estimation would require a correct definition of the pump intensity distribution and of its overlap with the intra-cavity field modes, in terms of a convolution integral.

In order to determine the maximum power extraction obtainable from these systems, Finite-Elements-Mesh (FEM) numerical simulations of the thermo-mechanical behavior of the slabs is the appropriate approach [6] taking into account the fracture limit stress of the active medium. In the following some examples of these calculations are reported in the case of the 1% doped slab described above.

The slab is modeled as face-pumped with uniform profiles along the  $z$  and  $y$  directions. The pumping power is assumed to decay exponentially in the  $x$  direction (3-mm-thick dimension of the slab) and, to evaluate the worst case of maximum thermal load, perfectly monochromatic light is considered, that means applying an absorption coefficient equal to the peak value ( $10 \text{ cm}^{-1}$ ). Such choice results in 95% absorption of the pump power in a single passage through the slab. On both slab opposite faces, the pump power is set to 500 W (1 kW total power) over an area 60 mm x 10 mm wide. These two areas are rigidly maintained at 20 °C to account for cooling by any flowing liquid from a chiller. The thermo-mechanical coefficients adopted in our simulations are summarized in Table I (note that these parameters apply both to crystalline and ceramic YAG [22, 23]).

A sample graphic result of FEM calculations is shown in Figure 3.

The main results of this computer simulation are the maximum temperature inside the slab (68 °C in this case) and the maximum mechanical stress ( $1.02 \cdot 10^8 \text{ N/m}^2$ ). The latter value indicates that, with such pumping-cooling geometry, 500-W pumping per side of the slab is 1.5–2.5 times below the fracture limit indicated by YAG crystal suppliers ( $2\div 2.5 \cdot 10^8 \text{ N/m}^2$ ) and at least 6 times below the fracture limit indicated for the polycrystalline ceramic YAG ( $10^9 \text{ N/m}^2$ ). Simulations can be repeated with different geometries to explore relevant changes in the thermal and mechanical load conditions. Figure 4 shows the results obtained

**Table I. Thermo-mechanical YAG parameters for FEM simulations**

Parameter	Units	Value
Young's Modulus	$\text{N/m}^2$	$2.82 \cdot 10^{11}$
Poisson Coefficient	–	0.28
Thermal Expansion Coefficient	$1/^\circ\text{C}$	$8.0 \cdot 10^{-6}$
Specific Heat	$\text{J/Kg } ^\circ\text{C}$	$5.9 \cdot 10^2$
Thermal Conductivity	$\text{W/m } ^\circ\text{C}$	10.7
Mass density	$\text{Kg/m}^3$	$4.55 \cdot 10^3$

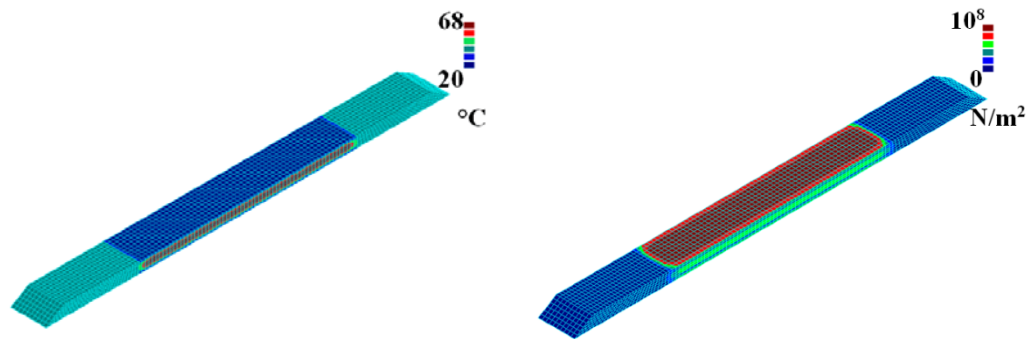


Figure 3. Temperature (left) and Stress (right) distributions calculated by FEM simulations on our slab geometry (for a 3 mm thickness).

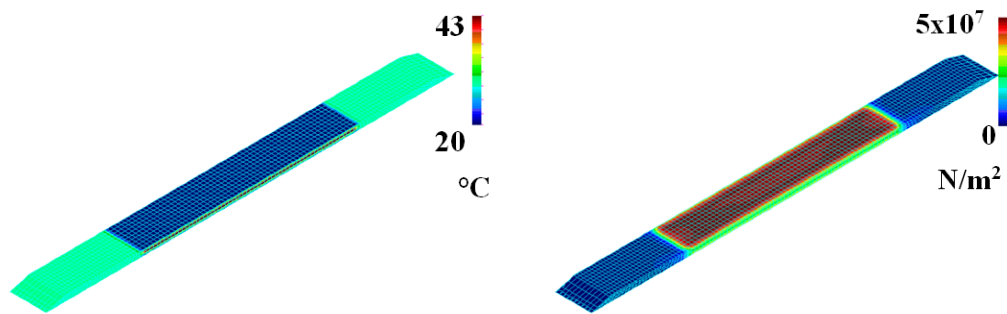


Figure 4. Temperature (left) and Stress (right) distributions calculated by FEM simulations on our slab geometry (for a 1.5 mm thickness).

with a slab having 1.5 mm thickness, assuming the same pumping power and a 2% doping level (in order to maintain the same average absorption). Due to the thickness reduction, cooling is improved and consequently the maximum temperature is reduced to 43 °C and the maximum mechanical stress to  $4.95 \cdot 10^7$  N/m<sup>2</sup>. This, in principle, would represent a significant benefit, facilitating higher diode pumping levels on the slab, at least up to 1 kW per side. It is clear, however, that higher doping reduces the radiative decay time of the upper level (from 230  $\mu$ s for a 1% doping to 175  $\mu$ s for 2% doping), thus reducing the optical-to-optical extraction efficiency of the laser [24]. Moreover, a 1.5-mm-thick slab would mean a higher number of internal reflections in the zig-zag optical path inside the ceramic, possibly increasing the round-trip losses and wave-front distortions.

This modeling is of course bound to the attainment of a reasonably uniform pumping distribution. A strong non-homogeneity of the pump radiation can cause internal cracking even at pumping power densities that are predicted to be safe by the above described modeling. Figure 5 shows the internal cracking of a 2% doped ceramic slab with dimensions equal to those considered in the FEM model previously described. The fracture was caused by the use of direct illumination of real diode arrays (two 600 W vertical stacks) without any homogenizing optics, at a level corresponding to an average pumping power density of 350 W/cm<sup>2</sup>.



Figure 5. Image of an internally cracked slab, because of internal stresses above the fracture limit.

### 3. Pumping Schemes for Slab Lasers

As already stated, high power diode laser bars have seen an enormous technical development over the last 10 years, and their power, stability, line-width and dimensions have been largely improved. These improvements stimulated many studies and experiments about new laser schemes, particularly suited both to exploit the best performance of these kinds of pump sources and to minimize the effects of the large thermal loading induced on the active medium as a consequence of the high absorbed power densities. The problem of designing the optimal pumping scheme for solid state lasers is then a key point that has been widely investigated for a lot of different active-medium types and geometries. In the case of rod lasers [12], diode pumping has been successfully adopted both in end- and in side-pumping schemes. The end-pumping produces an optimal pump radiation to fundamental mode overlap enabling the design of systems that can efficiently produce  $TEM_{00}$  radiation. Unfortunately, this scheme results in relevant thermal gradients and thus it can be adopted only for powers below 100 W. For high power applications the side-pumped systems are easily accomplished and diode pumping (often with adoption of highly reflecting chambers) allows an easy direct radiation coupling. The extracted beam quality is nevertheless very poor given the relevant thermal lens effect and thermally induced birefringence intrinsically produced by the radial cooling of the rod.

The disk laser [5, 15] is precisely aimed at solving the above mentioned problems. This system is a sort of short and fat rod laser that is cooled on (at least one of) its faces instead of being cooled on its lateral cylindrical surface. This can be done in a single-side cooled active mirror scheme [5], or in a more traditional cavity [15] with the disk cooled on both sides. The pump radiation is usually circularly symmetric, matched to the cavity mode, and often produced by a fiber homogenizing the diodes radiation. This geometry has the big advantages that (i) thermal gradients are minimized by the large surface-to-thickness ratio, and (ii), due to the coaxial pumping, they are parallel to the beam propagation path and thus they weakly affect its quality. Anyway, the reduced thickness of the active medium, necessary to obtain an effective cooling, requires a high doping of the active medium and/or for a multipass pump radiation absorption path. In addition, the resonator volume is necessarily much larger than

the active medium volume (in order to effectively extract a reasonable mode). As a consequence, the typical disk system turns out to be rather complex and the extremely high specific power-extraction makes several laser parts absolutely critical. This is the case of the thermal interface between the active disk and the cooler. Multi-kW disk lasers are now commercially available but based on long folded resonators with multiple active-disk elements, with the result of large system volume and complexity.

Fiber lasers have been recently proposed for high power laser applications, both adopting traditional end-pumping schemes [13] or adopting a more complicated Y-pumping technique [14]. The first advantage of these sources is the cooling system simplicity (sometimes air cooling is adopted) given the significant source length. Fiber lasers adopting the Y-pumping scheme or the groove pumping coupling also have the advantage of employing reliable low power diodes well established for telecommunication applications. The global system is thus characterized by a high modularity and redundancy but at the same time it shows a relevant complexity. Moreover, as in the case of disk lasers, lower beam quality still has to be accepted for multi-kW sources, since a mono-mode fiber core would not withstand the very high intracavity beam irradiance (the damage limit is estimated to be around  $1\text{W}/\mu\text{m}^2$ ). Multicore fibers are presently being investigated to enhance the power level of quasi-TEM<sub>00</sub> emission.

Slab lasers present the same advantage of disk lasers in reducing thermal gradients effects. A large cooling-surface to thickness ratio enables an efficient cooling of the active medium. High average power end-pumped slab lasers have already been studied in Refs. [8,17]. Coaxial pumping and cooling allows to further reduce the thermal distortions, and zig-zag propagation in the active slab limits the uniaxial thermal lens effect [16] averaging over thermal gradients. This can be easily understood considering that the thermal lens power in a rectangular geometry is given by [27], [28]:

$$\frac{1}{f} = \frac{Ql}{k} \cdot \frac{dn}{dT}, \quad (8)$$

where  $Q$  is the thermal power loading per unit volume,  $l$  is the slab length and  $k$  is the material thermal conductivity. Given the system symmetry  $dn/dT$  has a zero average along the  $x$  transverse direction thus in a zig-zag optical path rays suffer the same average phase retardation. In other words the zig-zag propagation eliminates the focusing effect at the first order.

Thus, design efforts can be devoted to the attainment of these conditions, that can be obtained in a laser based on a Nd:YAG slab, as those described in the previous paragraph, and face- or side-pumping schemes; face-pumping occurs if the pump radiation is directed towards the large  $L \times W$  slab surface, while side-pumping if the pump radiation impinges the thin  $L \times T$  surface.

A typical diode bar array well suited for direct face-pumping of the 1% doped, 114.2 mm long slab described in the previous paragraph is shown in Figure 6. It is organized as a horizontal sequence of six 2-bar stacks, each bar emitting a maximum of 50 W of QCW power in 160- $\mu\text{s}$  pulses with a pulse-repetition frequency up to 1 kHz. Naturally higher pump powers are obtained stacking a larger number of bars in each of the six elements, at least in a QCW regime.

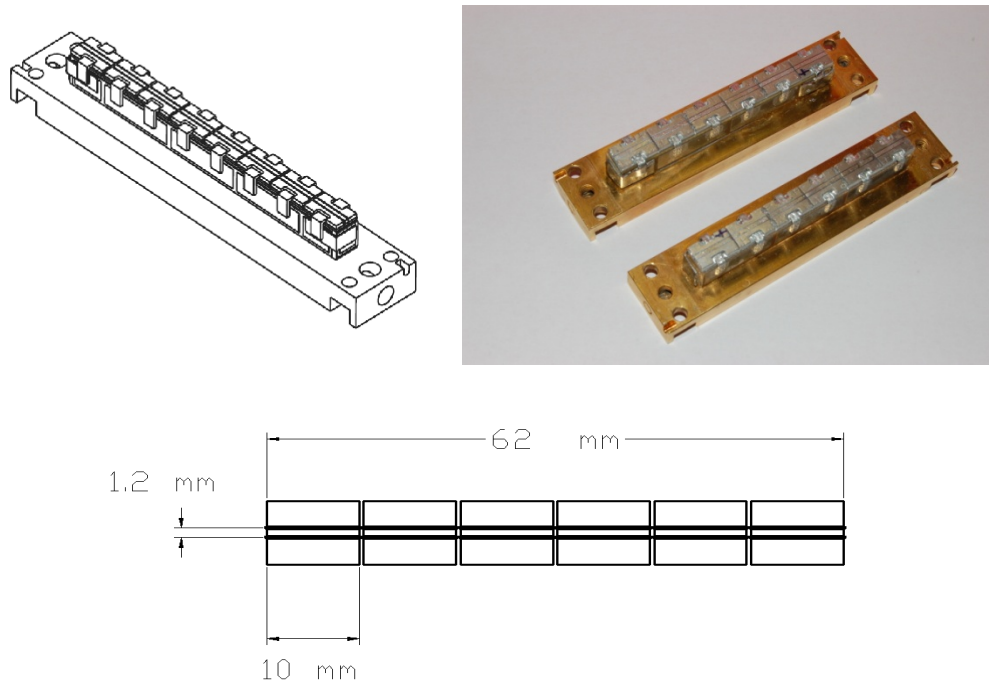


Figure 6. IMC Horizontal array of two-bar stacks.

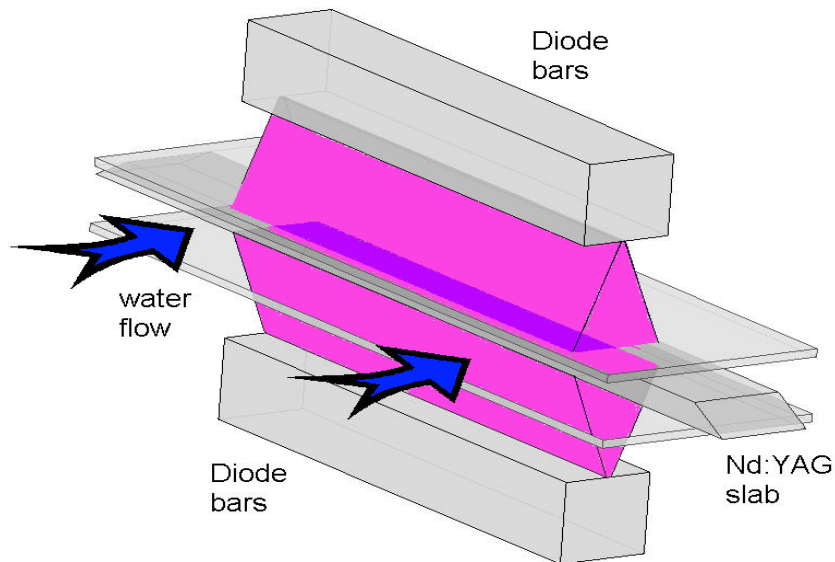


Figure 7. Schematic drawing of the horizontal diode array face-pumping geometry.

The bars, consisting of 72 emitters with a  $40^\circ$  fast axis divergence and a  $10^\circ$  slow axis divergence, are aligned along their longer dimension (slow axis of the laser diodes). As a consequence, each array represents a 600 W illuminator with an equivalent size of 1 mm x 60 mm and  $40^\circ \times 10^\circ$  divergence angles. These devices (Model ARR02P600 by Industrial

Microphotonics Company, St. Charles, Missouri) present the further advantage of being operated with indirect cooling through a rather large channel in the array base, so that no particular care should be taken in the cooling circuitry. The slab is mounted (by means of thin sheets of silicone seal) in an metal case between two quartz windows (low absorption @ 808 nm), as schematically depicted in Figure 7, and a thin layer of water (1.0 mm thick) is allowed to flow over the pumped side faces of the slab.

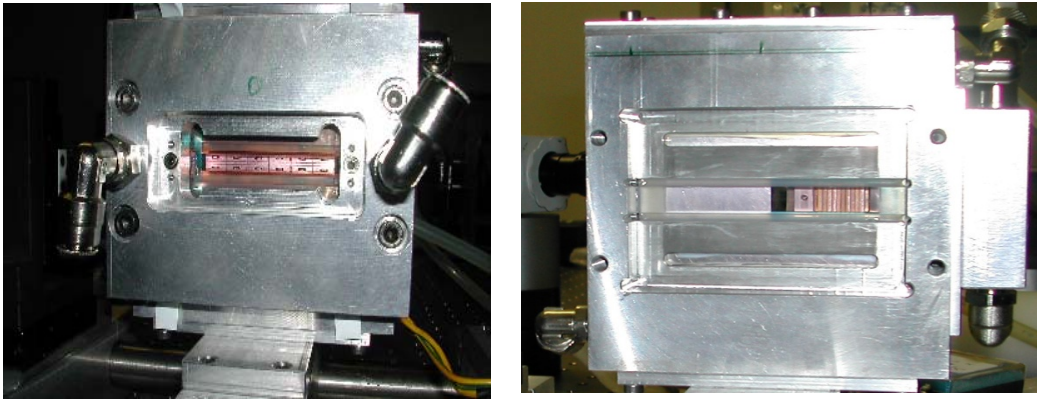


Figure 8. Photograph of the slab face-pumping unit equipped with horizontal (left) or vertical (right) diode assemblies.

Figure 8 shows the slab mounted in the experimental framework. Considering the geometry of the pumping beams and all the mechanical constraints, the arrays are settled at an optimal distance of 11 mm from the slab face, such that approximately 80% of the total emitted power is directly coupled to the active medium's side faces. Quartz windows are AR coated @808 nm on the front side, while negligible reflections remain at the two water-slab and water-quartz interfaces.

A first step to optimize pumping is to temperature tune the diodes to produce the highest laser emission. Figure 9 reports a typical sample set of measurements performed to optimize the pumping radiation wavelength. Direct optical gain measurements at 1.064  $\mu\text{m}$  have been performed with a 400-mW, single-mode probe beam generated by a Nd:YAG laser (Forte 1064, by Laser Quantum, UK). Values of single-pass gain versus water cooling temperature are shown in Figure 9(a); a maximum single-pass gain of 45% is obtained, corresponding to a linear gain coefficient of 0.06  $\text{cm}^{-1}$  (note that such values are found at 35 °C cooling temperature since the arrays of this experiment have been originally assembled for Nd:glass operation [6] @ 802 nm).

Since the water cooling system doesn't allow temperatures higher than 35°C we equipped the slab module with a simple two-mirror stable resonator cavity and run it without cooling fluid circulation for a short time (Figure 9(b)). A thermocouple was used to monitor the diode mounting-block temperature so that plots of extracted power versus diode mounting temperature could be obtained. Figure 9(c) shows two smooth maxima for the wavelength dependence of the output power that are related to the 805- and 808-nm peaks in the Nd-doped YAG absorption spectrum. The smoothness of these maxima is caused by the intrinsic and temperature-related spreads in the diode emission wavelengths, and to the Nd-ions

absorption of these different wavelengths. As a consequence we find that the extracted power varies not more than 30% in a large range (10 °C) of diode temperatures.

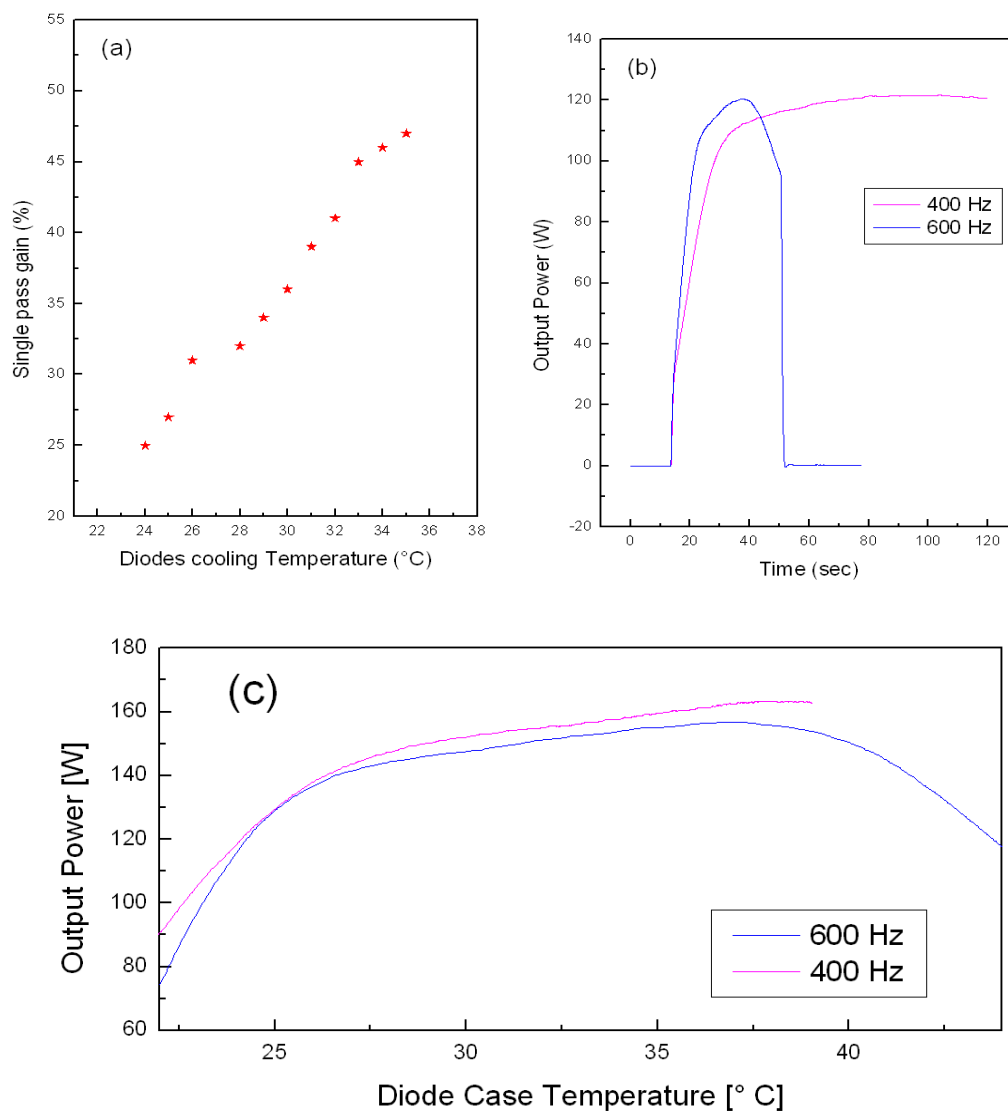


Figure 9. Single pass Gain versus diode cooling temperature(a).Cavity power extraction versus time (b) or diode case temperature (c) in the uncooled system runs.

A second step in the pumping optimization is to maximize the optical coupling between the diode array radiation and the slab active volume [18]. Even in the case of the best array-to-slab distance, the amount of radiation laterally lost in the y direction (corresponding to the diodes fast diverging axis) is not negligible, given the bell-shaped profile of the diodes emission lobe.

For this reason reflecting surfaces can be added to the pumping units, thereby confining the diode array radiation in the fast-axis direction. Figure 10 shows a schematic of a transverse section of the optical system with the resulting optical ray paths.

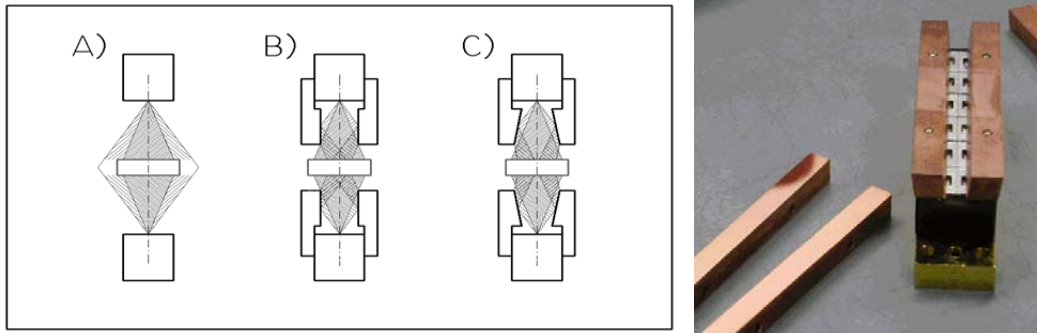


Figure 10. Schematic cross-sectional drawing and picture of the side copper reflectors used to guide the pumping radiation onto the slab face.

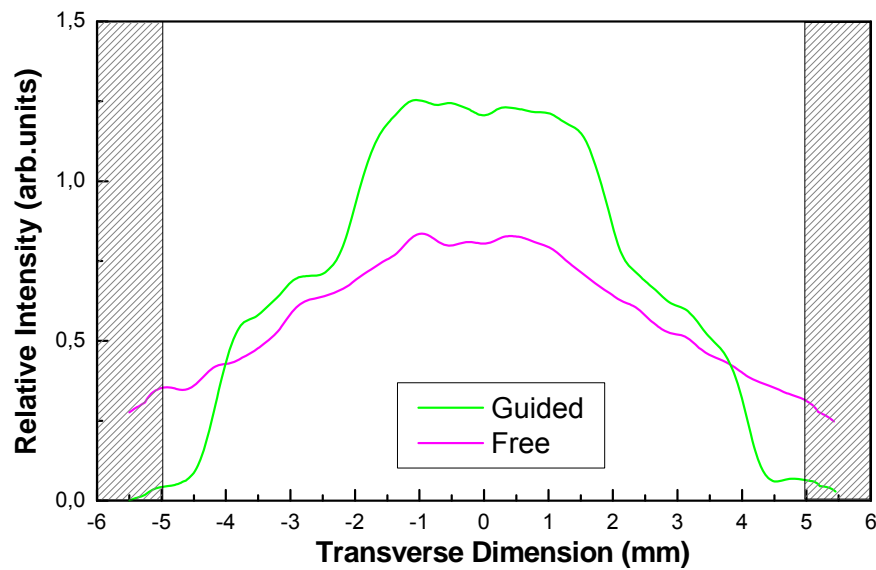


Figure 11. Calculated transverse intensity profiles of the pump radiation on the LxW face of the Nd:YAG slab, with side reflectors (green line) and without side reflectors (red line). The intensity falling in the dashed areas corresponds to the radiation that fails to hit the slab face.

It is clear from this figure that the reflectors act to enhance the fraction of diode emitted energy impinging on the slab face. With the aim of evaluating the improvements achievable with application of side copper reflectors, commercial ray-tracing packages can be employed successfully [18]. In order to study the problem of coupling in the x-y plane, the system can be considered as being translationally invariant along the longer slab direction (coinciding

with the laser axis). The diode laser array can be modeled as an almost pointlike source with an angular radiance distribution specified by the supplier. Given an angular sector, the software package draws a number of rays that are proportional to the irradiance in that sector. By counting the rays that reach a user-defined target (the slab face), the software allows the energy coupling coefficient to be calculated. The optical setup also has to include an aperture between the reflectors and the slab surface in order to account for the water-cooling layer and the quartz windows. The setup shown in Figure 10 (where flat reflectors extend for 8 mm from the diodes and leave a lateral aperture of 3 mm) has been numerically investigated for several values of different parameters, such as the diode-to-slab distance, reflector separation  $D$  (measured at half-extension, 4 mm) and reflector skew angle  $\theta$ . In all the calculations the duct wall reflectivity was set to 98.0%. Typical results of the calculated relative intensity profiles along  $y$  axis are shown in Figure 11 .

**Table II. Coupling Coefficient and Uniformity Factor obtained from photometric ray-tracing simulations**

Geometry	Coupling Coefficient (%)	Uniformity Factor (%)
Free propagation	70	31
Parallel flat reflectors <sup>1</sup>	94	53
Skewed flat reflectors <sup>2</sup>	98	41

1)  $D = 6$  mm,  $\theta = 0^\circ$ ,    2)  $D = 5$  mm,  $\theta = 10^\circ$ .

It is also useful to define an uniformity factor  $U$  for the pump radiation distribution along  $y$  as

$$U = \frac{\sigma}{\langle I \rangle}, \quad (9)$$

where  $\langle I \rangle$  is the average value of the irradiance impinging on the slab and  $\sigma$  is its variance. Given this definition, a lower  $U$  coefficient means a better uniformity of the pump radiation distribution. Table II reports the coupling coefficient and the uniformity factor obtained for the best coupling in the three optical configurations corresponding to Figure 10. Skewed flat reflectors ( $\theta = 10^\circ$ ) provide the best compromise between coupling efficiency and uniformity.

Verification of the effect of the reflective ducts in optimizing pump coupling is provided by observation of the fluorescence light at 1.064  $\mu\text{m}$ . To make this, a CCD video camera (with a 16 mm objective) and a personal computer frame grabber can be used. Direct imaging of the slab along the laser axis is obviously impossible, because the amount of diffused diode light reaching the CCD is much larger than the fluorescence intensity. Thus, the use of an interference filter (central wavelength, 1064 nm; half-width at half-maximum, 10 nm; peak transmittance, 85%) characterized by high rejection in the 808 nm region (better than 1:1000) is required. Given the typical value of the diode power ( $\sim 1000$  W), even direct fluorescence light would saturate the CCD detector and the use of a further attenuator is

necessary. The fluorescence images obtained in the three different configurations are shown in Figure 12.

Images were recorded and analyzed to extract the profile of the fluorescence irradiance distribution in the middle of the Nd:YAG slab and the resulting profiles are shown in Figure 13 which appears in good agreement with the numerical data of Figure 11.

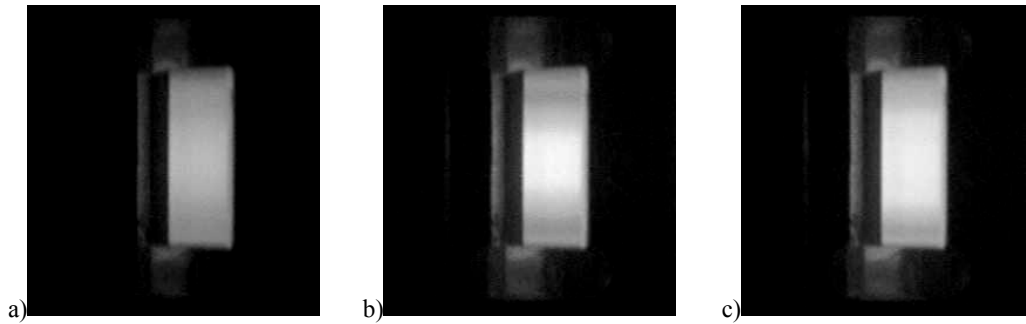


Figure 12. Experimental images of fluorescence when the ceramic slab is laterally pumped with a) diode arrays without reflectors, b) diode arrays with parallel copper reflectors, c) diode arrays with skewed copper reflectors.

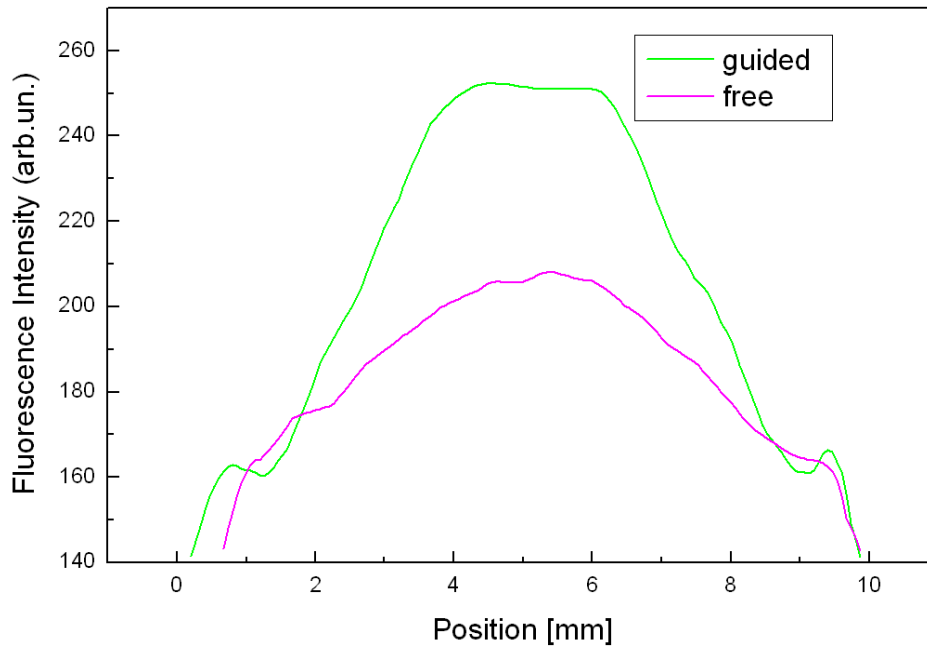


Figure 13. Experimental profiles of the ceramic slab fluorescence with side skewed reflectors (green line) and, without side reflectors (red line).

To confirm the validity of results the relative values of  $U$  can be compared. In fact, calling  $U_r$  the uniformity parameter obtained with parallel reflectors and  $U_f$  the uniformity parameter obtained with free-propagation coupling, the ratio  $R = U_r/U_f$  results to be  $R = 1.65$

for fluorescence measurements and  $R = 1.70$  for numerical ray-tracing simulations, respectively. A quantitative description of the positive effects on the laser power extraction and slope efficiency due to the introduction of side reflectors is reported in the next paragraph.

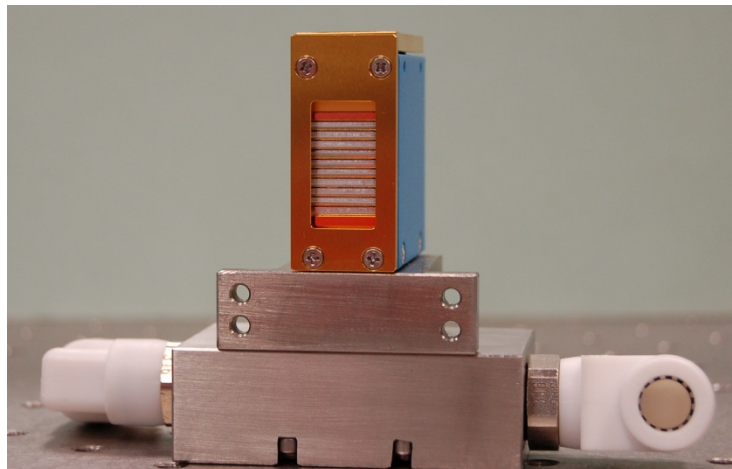


Figure 14. Vertical stack of high power diode bars: Jenoptik (mod. Jold-500-cann-10A).

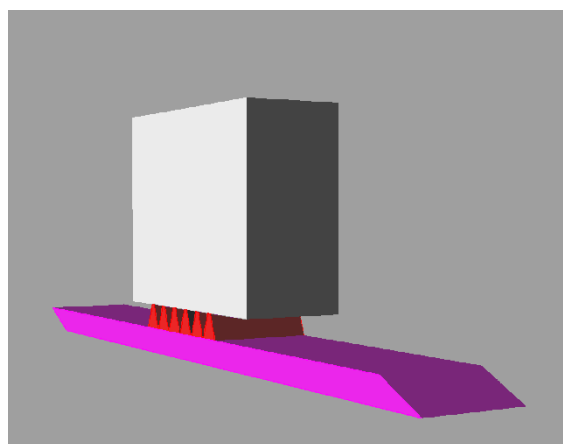


Figure 15. Slab laser face-pumping with a vertical stack of high power diode bars.

Another diode configuration that can be fruitfully adopted for YAG slab face-pumping consists of a number of diode bars that are vertically stacked to produce a compact square or rectangular illuminator, as shown in Figure 14 [25].

In the case of the device of the Figure 14, 10 bars are stacked with a pitch of 1.8 mm, to obtain a 600 W power source with 10 mm x 18 mm dimensions. The typical one-sided pumping scheme with a simple free space propagation is schematically presented in Figure 15. Since the diode fast divergence angle is now oriented along the  $z$  axis, emission lobes of the different bars are well superimposed. The resulting spatial distribution of the pump light is sufficiently uniform, and only a reduction of the diode-to-slab distance is required to obtain a

very good pump coupling. The amount of radiation laterally lost is negligible since the  $y$  direction corresponds to the diodes slow diverging axis.

With respect to horizontally stacked arrays, vertically stacked ones present the disadvantage of requiring an active cooling that is a direct water cooling by means of internal micro-channels. Deionized clean water is necessary and much care must be taken to satisfy flow and pressure drop specifications to avoid overheating or water leaks through the gaskets separating next neighbouring bars.

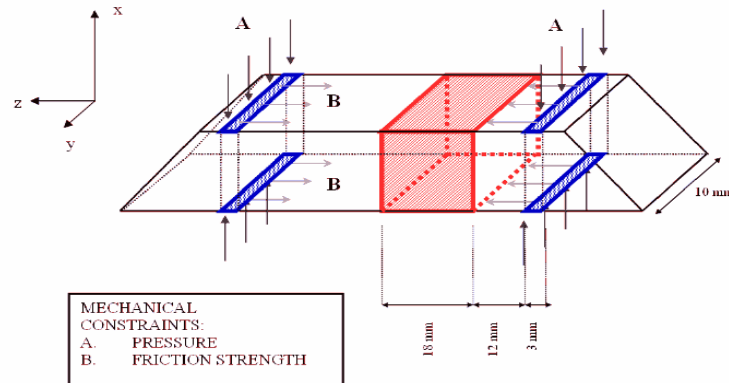


Figure 16. Geometrical scheme of a complete thermo-mechanical model of the face-pumped slab. Localized mechanical constraints are taken into account including possible friction asymmetries.

A practical limitation of a face-pumping scheme arises from the difficulty to apply efficient mechanical constraints to the slab, since most of the two large  $L \times W$  surfaces have to remain clear for pumping and cooling. Whenever a certain value of the pumping power density is exceeded ( $\sim 750 \text{ W/cm}^3$ ), slab deformations (such as bending for instance) appear that causes a degradation of the optical cavity and thus results in consistent instability of the laser output.

Preliminary investigation of thermo-mechanical management of face-pumped gain unit can be performed by FEM simulations as reported in the previous paragraph with the addition of mechanical constraints [29]. In our case, the 114.2 mm long, 1% doped YAG slab is sustained in the mechanical frame of Figure 8 by means of 4 rubber stripes (the water cooling chamber gaskets) subject to a normal compression. Figure 16 represents schematically the gain unit (slab length  $L$  not in scale); one-sided and both-sided face-pumping with a couple of 600 W vertical diode stacks has been considered, as this configuration (with the most concentrated pump power density) will induce the highest thermal loading.

Results of numerical simulations show that if the same compression is applied to the gaskets, the slab expands mainly along the  $z$  direction without distortions. Since in practical reality the compressing forces cannot be distributed with perfect uniformity, a different friction between the gasket and the slab surfaces is to be considered. We introduced this symmetry break in our simulations by setting a different value of the elasticity modulus for each gasket. The main results of numerical calculations are reported in Figure 17, a case-study where an asymmetry is introduced between the elasticity modulus of the rubber stripes

above the slab ( $E_{\text{up}} = 10^9 \text{ N/m}^2$ ) and below the slab ( $E_{\text{down}} = 10^7 \text{ N/m}^2$ ). Figure 17 gives particular evidence of the slab bending caused by combined thermal load (450 W pumping power from each unit) and constraints asymmetry.

In order to validate the numerical results and characterize distortions induced by thermal loading, the experimental face-pumped gain unit has been inserted in a Mach-Zehnder interferometer as reported in Figure 18. The He-Ne laser beam has been expanded to 40 mm diameter and accurately collimated. The two interfering beams are first aligned along the same axis, then the reference beam (free propagation) is slightly tilted with respect to the object one (passing through the slab), so that a linear pattern of fringes is generated. A CCD camera (equipped with 633 nm center-wavelength interference filter) records the fringe patterns as shown in Figure 18.

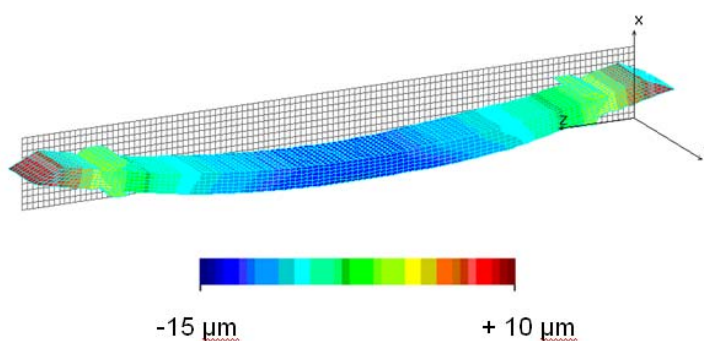


Figure 17. Results of the Thermo-mechanical modeling: geometrical deformations of the slab pumped with equal power from both sides (450 W each side), but with asymmetric constraint friction.

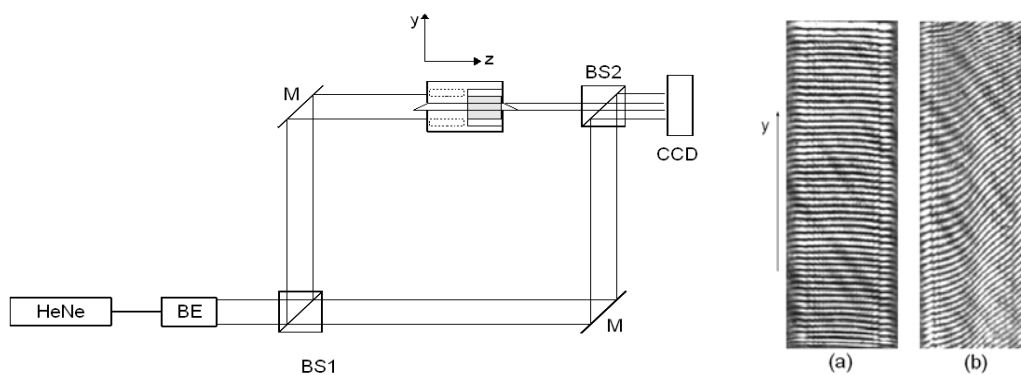


Figure 18. Experimental diagnostic set-up, based on a Mach-Zehnder interferometer, adopted to characterize the slab deformations. The recorded fringe patterns are also shown for the cold (a) and hot (b) slab conditions.

In absence of pumping the fringes are parallel and equally spaced, while in presence of diode radiation (350 W on both sides in the example of Figure 18) the fringe pattern becomes irregular as a consequence of slab deformation induced by thermal loading. The information on wavefront distortion can be retrieved by standard Fourier-transform and filtering procedures. The initial phase map (pump diodes off) is subtracted to successive phase maps, so that differential phase change  $\Delta\phi(x,y)$  due to the slab deformation can be obtained. The interpretation of results is performed with reference to a linear expansion over a set of standard aberration components [29].

$$\Delta\phi(x,y) = A r^4 + Bx r^2 + Cy r^2 + D(r^2 + 2y^2) + Er^2 + Fy + Gx + H, \quad (10)$$

$$r^2 = (x^2 + y^2). \quad (11)$$

The above polynomial expression is fitted to experimental wavefronts with A to H as free parameters, according to a linear least-square fitting procedure; the small value of residuals confirms that the chosen base set is capable of including all the relevant features.

Considering T and W the apertures determined by the rectangular cross-section of the slab in the x and y directions respectively, the maximum Optical Path Difference ( $OPD_{\max} = \Delta\phi_{\max} \lambda / 2\pi$ ) of each aberration in the case of a total pumping power of 700 W (350 on each side, corresponding to a diode drive current of 45 A) is reported in Table III.

As already seen by finite element calculations, these results confirm that x- and y-tilts are dominant and can be easily evaluated to be of the order of 2-3 mRad as the ratio between OPD and slab transverse dimensions. As regards thermal lens effect, the following relation can be used

$$ROC = a^2 / 2 \text{ OPD}, \quad (12)$$

where ROC is the wavefront Radius Of Curvature, and a is the wavefront semi-aperture. Extremely large focal length values ( $ROC_y = 6.25$  m) for the slab lateral direction confirm the negligible thermal gradients produced by this geometry along the y axis. On the contrary, the strong thermal gradients in the thin transverse dimension produce a more sizable lens effect in the x direction, in spite of the zig-zag averaging process. The focal length on the x axis reaches values as small as 380 mm at the maximum power loading.

Figure 19 also shows the temporal evolution of the aberration coefficients F and G in the first two minutes of diode operation. Interestingly, two different time scales are visible in the transient measurements. A short one (1-2 seconds) in which the slab absorbs light, expands and experiences mechanical constraints; y-tilt is completely set in such a time. A longer one (1-2 minutes) in which heat diffusion towards the slab cooled surfaces generates thermal gradients; x-tilt is almost totally due to this phenomenon. All the above observations reveal that, for high pumping levels and related intense thermal loading, the laser efficiency is much more limited by thermally induced slab bending rather than thermal lensing. The corresponding beam tilt produces an aperturing effect which implies a worst beam to active medium coupling and extra cavity loss contribution.

A different way to obtain an efficient pumping of the slab active media is called the edge-pumping configuration and is shown in Figure 20 [26, 30]. A sample case of this scheme is represented by the “*parallelogram shaped*” YAG slab reported in a paper of ours [26] and that has the following dimensions: L = 37.8 mm (edge-to-edge), W = 20 mm, T = 4 mm. The slab has a 0.6% Neodymium doping, and, given the edge-pumping configuration, it can be

sandwiched on the two  $L \times W$  large faces with indium foil between two metal plates maintained at fixed temperature by tap-water cooling. Of course, such mechanical mounting is simpler and more stable than that adopted for face-pumping, allowing stronger and more uniform mechanical constraints. On the other hand, the pumping radiation input surfaces are narrow and long in edge-pumping scheme.

**Table III. Maximum OPD for each aberration @ 700 W pumping level**

Aberration	Polynomial	OPD <sub>max</sub>
y-tilt	Fy	20 $\lambda$
x-tilt	Gx	10 $\lambda$
Sagittal coma	Cyr <sup>2</sup>	7 $\lambda$
Spherical aberration	Ar <sup>4</sup>	5 $\lambda$
x-defocusing	(D + E)x <sup>2</sup>	3 $\lambda$
y-defocusing	(3D + E)y <sup>2</sup>	2 $\lambda$
Tangential coma	Bxr <sup>2</sup>	0.1 $\lambda$

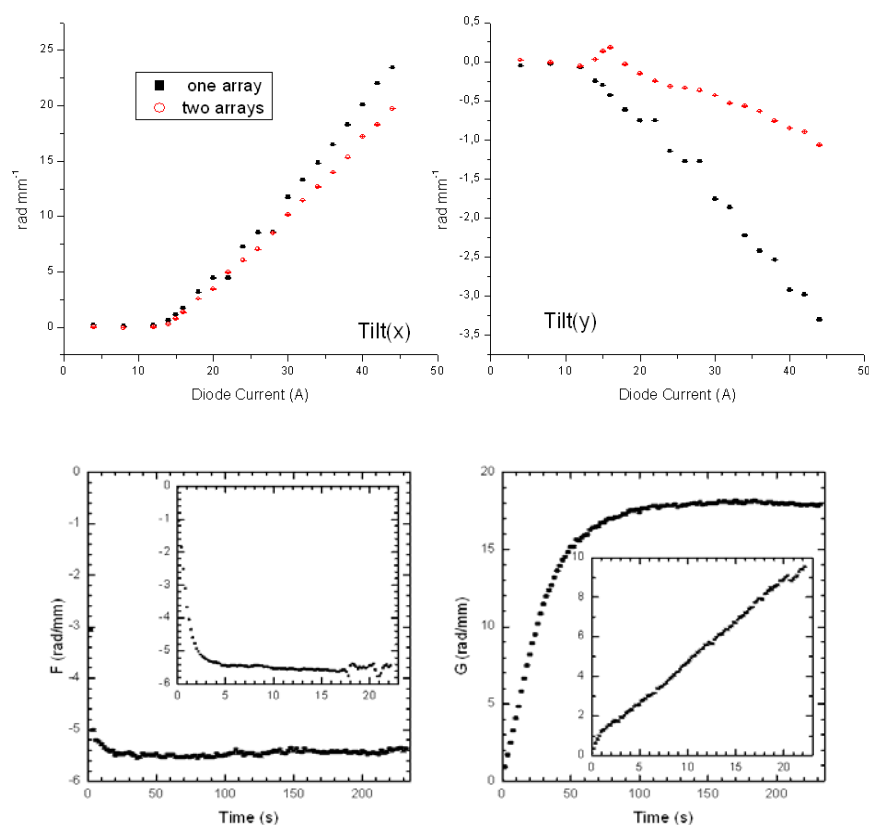


Figure 19. Stationary and transient tilt aberration terms measured on the face-pumped ceramic slab. Stationary measures show the linear dependence on the pump power (or diode current) while the transient plots give evidence of the different time scales on which the deformations build up.

Thus the optimal exploitation of high-power multiple-bar arrays requires the adoption of optical components aimed to concentrate the diode pump radiation. Even in close coupling conditions, at least the correction of the diode fast-axis strong divergence is needed. For the slab of our case study, pumping is achieved by the four laser-diode vertical stacks (model LT5500 by Lasertel [31]) of Figure 21. Each stack consists of five bars 0.4 mm spaced (the illuminator size is 2 x 10 mm) and delivering up to

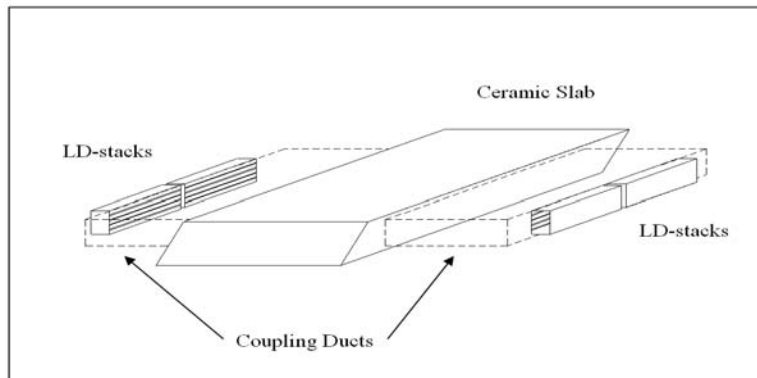


Figure 20. Schematic view of the edge-pumping configuration.

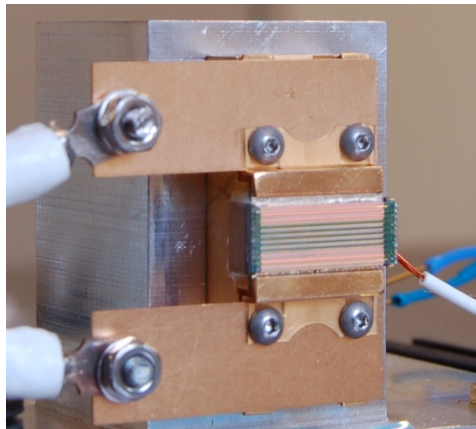


Figure 21. Vertical QCW stacks of collimated Lasertel diode bars

Of course, such pumping efficiency can also be improved by different kinds of optical ducts. A simple type consists of a hollow 3.5 mm x 25 mm wide spectralon channel, which, placed very close to the stack output, enables one to both increase and homogenize the radiation impinging the slab lateral face. Moreover, by the use of commercial ray-tracing packages (for example Trace-Pro, by Lambda-Research [32]), more complex BK7 optical ducts can also be designed. Figure 22 shows an optimized light concentrator consisting of a cylindrical lens (plano-convex, ROC= 30 mm) glued to a pyramidal prism; the input transverse section is 25 mm x 3 mm wide, while the output one has 1.5 mm x 15 mm dimensions. Placed with the lens vertex 5 mm far from a couple of stacks horizontally aligned

as in Figure 20, the duct is capable of concentrating onto the output surface roughly 90% of the power emitted by the diode stacks.

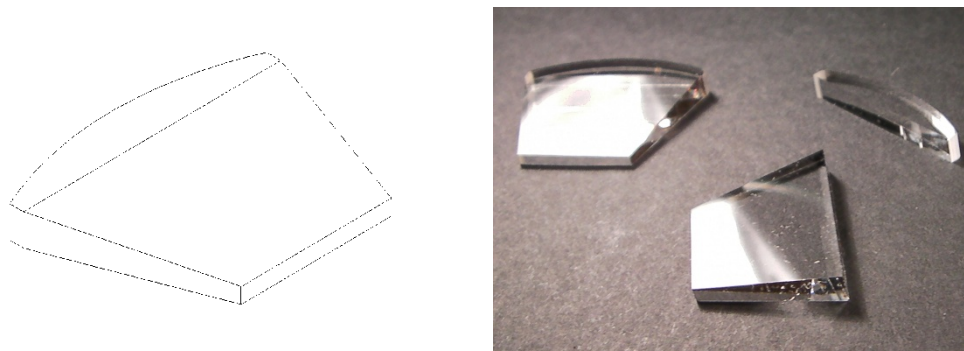


Figure 22. Drawing and photo of the BK7 optical concentrators acting as coupling ducts.

Another interesting feature of edge-pumping configuration is that temperature tuning of pumping devices is less important than in face-pumped lasers. The extraction characteristics are expected to be rather independent from laser diode cooling temperature, over a range of ten °C (as it will be shown in the next paragraph). This behaviour is mainly related to the long absorption path (20 mm in our case) characteristic of edge-pumping and the consequent large amount of absorbed power, also in the case of significant detuning of pump light from the main Nd absorption wavelength. For the same reason, it is also possible to obtain efficient pumping by using diode arrays with broad emission linewidths. In order to characterize this feature, it is interesting to calculate the fraction  $F(\delta)$  of pump power absorbed at a given penetration distance  $\delta$  from the slab input surface following the expression

$$F(\delta) = 1 - \frac{\int I(\lambda) e^{-\alpha(\lambda)\delta} d\lambda}{\int I(\lambda) d\lambda}, \quad (13)$$

where  $\alpha(\lambda)$  is the absorption spectrum of Nd:YAG and  $I(\lambda)$  the spectral distribution of the emitted intensity. Table IV reports some numerical results obtained via Eq. (13), for  $\delta = 3$  mm (face-pumping case) and  $\delta = 20$  mm (edge-pumping case). The YAG absorption spectra  $\alpha(\lambda)$  are measured by an infrared spectrophotometer (model *Lambda 900* by Perkin-Elmer) for 0.6 % and 1.0 % doping levels. The 3 nm-wide emission spectra  $I(\lambda)$  of the stack of Figure 21, have been measured by a fiber-coupled solid-state spectrometer at the maximum driving current; peak wavelength has been tuned in our experiments by changing the cooling temperature (approximately 0.25nm/°C).

For both doping levels, the maximum absorption has been obtained @ 808 nm peak wavelength. For  $\delta = 3$  mm, the absorbed power is doubled from 803 nm to 808 nm, thus confirming the role played by temperature tuning in face-pumped lasers. For  $\delta = 20$  mm the same wavelength variation induces only a 19% increment in the case of 0.6% doping and 10% increment in the case of 1.0% doping, which explains the lower temperature sensitivity of edge-pumped lasers. Moreover, the data of Table IV demonstrate that, as a consequence of the diode-bars linewidth, an “effective” absorption coefficient  $\alpha_{\text{eff}}$  for Nd:YAG can usually be considered, much smaller than the absorption spectrum peak value; referring to the values

obtained for  $\delta = 3$  mm @ 808 nm, we obtain  $\alpha_{\text{eff}} = 2.1$  cm<sup>-1</sup> for 0.6% doping and  $\alpha_{\text{eff}} = 3.2$  cm<sup>-1</sup> for 1.0 % doping, respectively.

**Table IV. Absorbed power fraction**

Doping	Peak wavelength (nm)	F( $\delta = 3$ mm)	F( $\delta = 20$ mm)
0.6 %	808	0.465	0.914
	807	0.415	0.900
	806	0.377	0.888
	805	0.359	0.870
	804	0.308	0.817
	803	0.226	0.724
1.0 %	808	0.620	0.956
	807	0.571	0.947
	806	0.531	0.942
	805	0.508	0.933
	804	0.442	0.905
	803	0.334	0.851

#### 4. Optical Resonators, Extraction Efficiency and Beam Quality

Probably the most crucial trade-off a laser designer has to face is the one between extraction efficiency and good optical quality of the extracted beam, primarily important in determining the focusability of the beam itself. For this reason the extraction capability of each slab gain unit is to be considered in relation to the optical resonator that will be coupled to it. Nevertheless it is of extreme importance to perform experimental efficiency tests based on the use of simple two-mirror stable resonators capable of extracting power from the whole active medium volume in a largely multi-modal field distribution.

The experimental data one obtains in this way yields important information on the attainment of an efficient pumping of the gain medium. Figure 23 for instance shows the power extraction characteristics of the face-pumped unit described in the previous paragraph and schematically depicted in Figure 7.

The laser cavity is 150 mm long. It consists of a concave spherical mirror with Radius Of Curvature (ROC) 500 mm and a flat partially reflecting out-coupler. Such geometry corresponds to a stable circularly-symmetric cavity. Different radii of curvature and cavity lengths have been tested, but those described hereafter give the maximum power extraction, indicating that the sustained laser mode gives the best filling of the inverted slab volume.

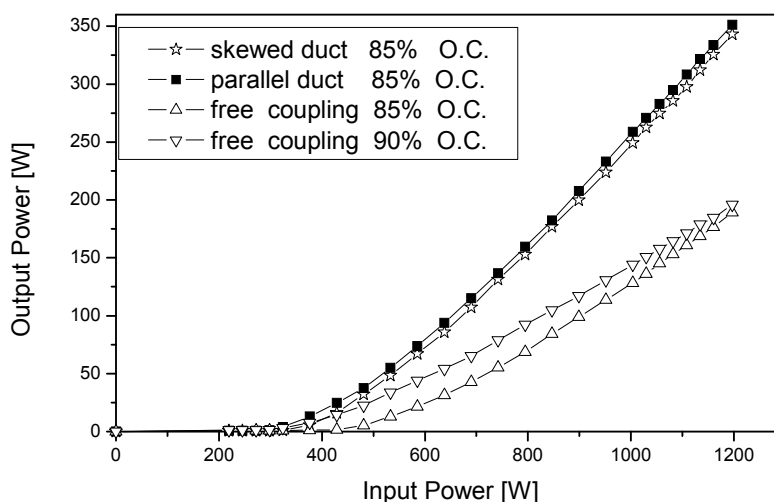


Figure 23. Extraction efficiency of the ceramic slab of Figure 2(left) Face-pumped by the horizontal stacks of Figure 6 with and without the ducts of Figure 10.

The different curves refer to different output coupler transmission coefficients and to different diode-to-slab optical couplings (free or guided as described in the previous section). Laser threshold is in the range of  $200 \div 300$  W. From these curves one can draw useful considerations. The use of duct coupling for instance improves the optical to optical conversion efficiency from 16% to 29%. Even more interestingly the slope efficiency is increased from a 26% of the free-propagation coupling to a 42% of parallel duct coupling to the 46% of the skewed duct coupling, this last value peaking up to a maximum value of 51% if the input pump power range from 1 kW to 1.2 kW is considered [18]. These values can be compared with the upper theoretical limit determined considering the product of the Stokes shift ( $\eta_s$ ) and the quantum efficiency ( $\eta_q$ ). For a Nd:YAG laser system [11],  $\eta_s=0.76$  can be simply calculated as the ratio between the energy of the absorbed and of the emitted photons, while  $\eta_q=0.95$  is related to the ratio of excited level decay times towards lower laser level and ground state. The obtained peak value of slope efficiency corresponds to 75% of  $\eta_s \eta_q$  and indicates a fairly good optimization of the pumping system in its geometrical and spectral aspects. Data reported in Figure 23 refer to a Quasi-CW regime [18]. In this way the extraction efficiency is not limited by thermo-mechanical distortion effects and can better characterize the pumping system effectiveness.

Clearly the beam extracted from a large Fresnel Number ( $N_f$ ) stable resonator will present very poor optical properties; given our slab transverse dimensions  $N_{fx} \sim 15$  and  $N_{fy} \sim 170$ . As a consequence of this, the beam produced with such a resonator presents a Beam Parameter Product of the order of 3 mm.mrad ( $BPP_x$ ) in the thin transverse direction and of the order of 30 mm.mrad ( $BPP_y$ ) in the lateral direction [6]. Since the  $M^2$  factor can be defined as the BPP divided  $\lambda/\pi$  (that is the beam parameter product of a fundamental Gaussian beam), the above BPP values correspond to  $M^2$  values of the order of 100 in the lateral ( $y$ ) direction and of the order of 10 in the transverse ( $x$ ) direction, and produce a relatively scarce focusability at least in the lateral direction. To overcome this problem one has to use optical resonators that

reduce the transverse mode content in the slab larger cross-section direction. Because of diffraction effects this can be accomplished using resonators with a reduced  $y$ -section, or, in other words, a reduced  $Y$ -Fresnel Number (Equivalent Fresnel Number in the case of unstable resonators [33]). This is the case of a Hybrid Stable-Unstable Resonator (HSUR), whose  $y$ -direction transverse scheme is depicted in (b) of Figure 24, or of a Multipass Folded Stable Resonator (MFSR - scheme (c) of Figure 24). These resonators can drastically improve the beam quality obtainable from the ceramic slab laser, naturally at the expense of the power extraction efficiency.

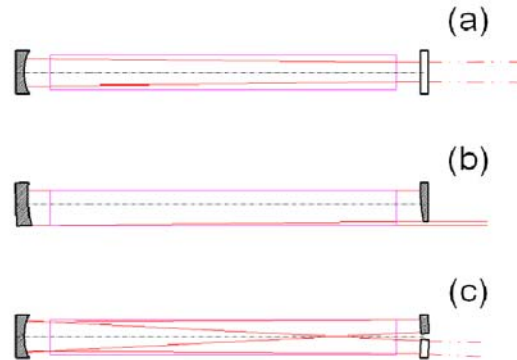


Figure 24.  $Y$ -direction transverse scheme of principle of three different resonators used with the slab ceramic lasers: (a) multimodal stable resonator, (b) Hybrid Stable-Unstable Resonator (HSUR) and (c) Multipass Folded Stable resonator (MFSR).

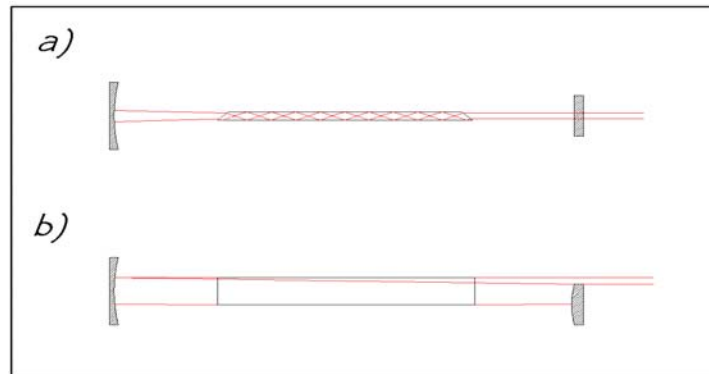


Figure 25. The Hybrid Stable Unstable Resonator coupled to the zig-zag slab. (a) Transverse direction view, (b) lateral direction view.

In the following the beam properties and conversion efficiency are described for two of our slab lasers equipped with a HSUR and a MFSR respectively. The optical scheme and principal rays path of the HSUR are shown in Figure 25 for both the thin zig-zag transverse direction (a) and the large lateral direction (b). In our experiments a negative-branch unstable resonator was adopted to avoid the high intracavity intensity regions (focal spots) in the ceramic slab volume that are generated by positive branch configurations [34]. The two

totally reflecting mirrors are a concave spherical (1.25 m ROC) mirror and a convex cylindrical (1.0 m ROC) one. The beam is coupled out of the resonator through an aperture determined at one side of the cylindrical mirror with a cross section 3 mm x 2.5 mm wide, in the x and y directions, respectively.

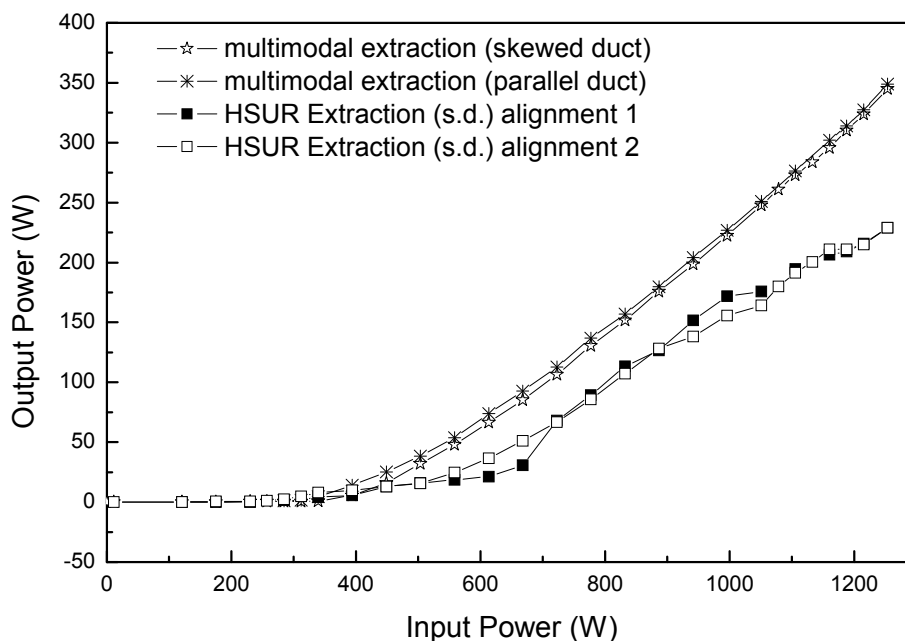


Figure 26. Power extraction curves for the zig-zag laser equipped with the HSUR.

Power extraction efficiency curves are reported in Figure 26 obtained with this resonator and compared to the maximum extraction obtained using the large multimodal resonators. Around 65% of the power obtained in multimodal emission, is extracted by this HSUR (at a conversion efficiency level of 19% and a with a slope efficiency equal to 29%) in a beam with extremely improved propagation properties. Different extraction curves are obtained for slightly different resonator alignments given the diffractive character of the output coupling adopted with this kind of resonator [34], [35].

The Near-Field transverse profiles of the extracted beam have been acquired using a linear array of pyroelectric sensors (Spiricon LP-256-11, spatial resolution 100  $\mu\text{m}$ ) [35] and are shown in Figure 27.

The profiles show a typical structure of a multi-mode Hermite-Gauss like beam along the stable direction, possibly with different lobes. Lobe number and intensity result strongly dependent on the resonator alignment conditions. In the unstable-transverse direction the profile is instead characterized by a fringe-like rippling of an almost flat-top intensity distribution typical of hard edge coupled resonators [34].

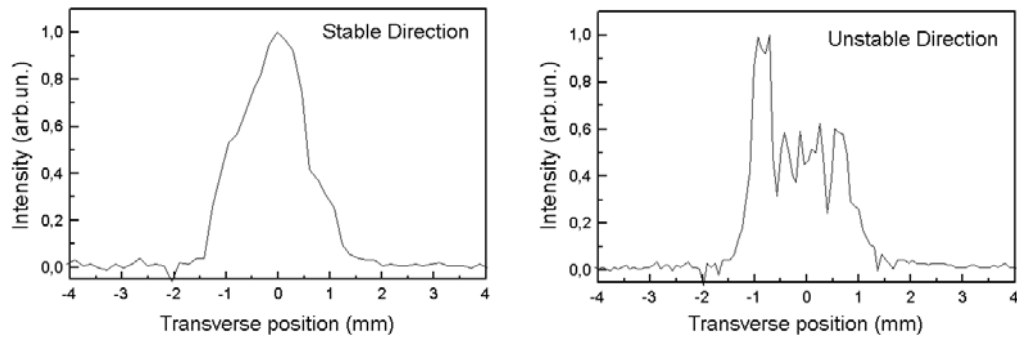


Figure 27. Near-Field Intensity profiles of the beam extracted from the HSUR: in the Stable Direction (x) and the Unstable Direction (y) respectively.

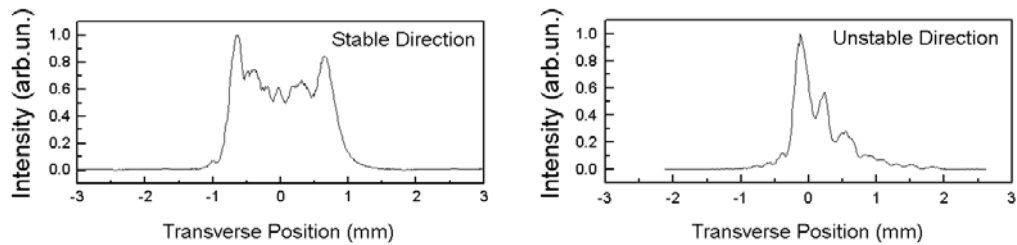


Figure 28. Far-Field Intensity profiles of the beam extracted from the HSUR: in the Stable Direction (x) and the Unstable Direction (y) respectively.

Correspondingly typical Far-Field Intensity profiles are reported in Figure 28, for the two different transverse directions. These profiles have been recorded in proximity of the focal plane of a converging lens with effective focal length of 700 mm, placed 1700 mm far from the laser output. In the stable direction (left picture of Figure 28) the far-field distribution shows the typical features of a mixture of low-order Hermite-Gauss modes. In the unstable direction (right picture of Figure 28) the far-field distribution consists of an almost diffraction-limited principal lobe followed by several secondary peaks produced by diffraction from the sharp edge of the output mirror.

A thorough beam propagation analysis was carried out on this kind of output to assess the beam quality improvement in the lateral transverse direction ( $y$ ) with respect to the case of simple multimodal stable resonators [35, 36]. Experimental measurements of the beam propagation parameters have been performed [35] following standard knife-edge methods [37] for the measurement of the beam diameter at various distances in a focused propagation path. Whereas a theoretical analysis of the beam properties in the unstable resonator transverse direction has also been performed [36] making use of numerical algorithms based on Fresnel diffraction integral propagations. This numerical approach enabled both the computer simulation of the resonator modal discrimination, in terms of spatial distribution and round trip losses, and the reconstruction of the resulting beam propagation properties.

Figure 29 clearly shows a better beam focusability for the Unstable direction ( $y$ ) than for the Stable direction ( $x$ ).  $M^2$  values calculated from the knife-edge measured beam diameters [37] range from 2 to 6 for the  $M_y^2$  and from 8 to 9 for the  $M_x^2$ . Interestingly the  $M_y^2$  values appear to grow linearly with increasing diode currents, or in other words with increasing slab laser output powers [35] reaching levels (around 6) sensibly higher than what one may expect given the diffraction limited width of the principal far-field lobe produced by the unstable resonator. This fact is to be attributed to the increasingly relevant role played by the secondary diffracted lobes present in the unstable direction far-field profile (see Figure 28). These peaks sensibly rise the “beam diameter” estimation based on the knife-edge method [37]. Given a natural noise-related minimum detectable intensity level, the relevance of the secondary peaks in determining the experimentally measured beam diameter grows with the beam power level and eventually affects the  $M_y^2$  estimations. This fact is evidenced in Figure 30, where  $M_y^2$  values (obtained from computer simulated beams [36]) are plotted versus the amplitude threshold, namely the minimum intensity level used to evaluate beam width. Amplitude threshold is expressed in terms of the relative fraction of peak intensity. Numerical analysis includes investigation of confocal and non-confocal resonators, corresponding to a cavity length of 125 mm (one half the difference of the mirrors radii of curvature) and to cavity lengths of 175 mm and 225 mm, the latter being actually the one adopted in our experimental system [35, 36]. Moreover, a  $\pm 100$   $\mu\text{rad}$  tilt angle of the spherical mirror has also been considered in the analysis. According to the results produced by the numerical simulations, the  $M_y^2$  value increases with decreasing threshold, giving evidence of the effect of the inclusion of secondary side peaks contributions, and  $M_y^2$  up to 5÷6 result indeed possible for non-confocal configurations. The two insets of Figure 30 report the encircled energies as a function of the Times Diffraction Limited (TDL) factor,  $\text{TDL} = 1$  corresponding to the diffraction angle of the fundamental Gaussian beam. Despite the relatively large values of  $M_y^2$  obtained, optical set-ups are possible that produce beams with more than 85% of the power falling within an angle 1.5 times the diffraction limit.

An alternative way to increase the extracted beam quality in the slab lateral direction is that of adopting a Multipass Folded Stable Resonator (MFSR). This choice may be favorable when requirements on the beam quality are not too stringent. For instance a Nd:YAG laser with a Beam Parameter Product equal to 3 mm.mrad can be easily coupled into a standard (N.A. = 0.2) 100  $\mu\text{m}$  fiber, with negligible losses [38]. Such a beam parameter product corresponds for a 1.064  $\mu\text{m}$  source to an  $M^2$  slightly lower than 9. When launching the beam into the fiber the beam produced by the MFSR has two advantageous properties: 1) a fraction close to one of the power is contained within the central far field lobe, that means a higher coupling efficiency 2) in case of a moderately multimodal beam no hot spots (i.e. high intensity peaks) are present in the field distribution, that means less damage problems on the fiber entrance facet.

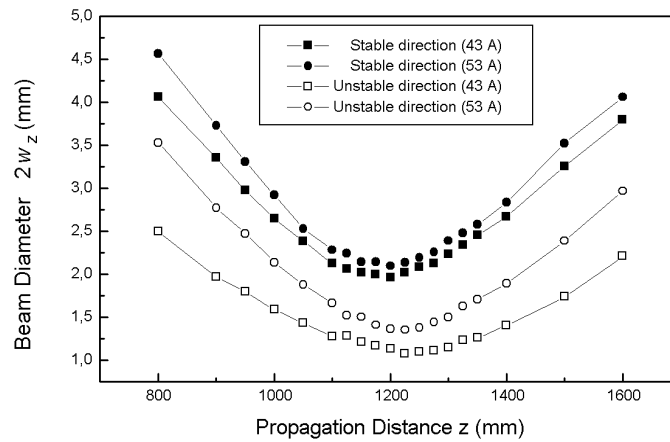


Figure 29. Propagation Caustics of the beam extracted from the HSUR.

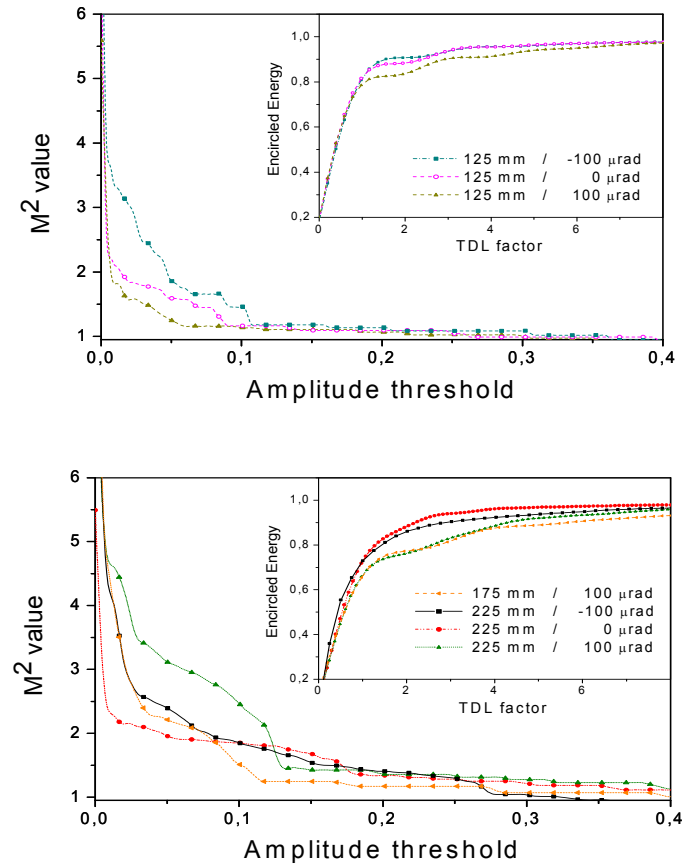


Figure 30. Propagation Quality Characterization for the beam extracted from the HSUR, for confocal configurations (above) and for non-confocal configurations (below).

The MFSR has been adopted in combination with the edge-pumped slab shown in Figure 20 and described in the last part of section 3. Given the large lateral size of the slab,  $W = 20$  mm, a stable, two-mirror resonator presents several drawbacks. The transverse Fresnel Number is very high, unless a long unpractical cavity is adopted. Moreover, due to the lower pump density in the central region of the slab, the resulting mode presents a rather uneven profile. Thus, a folded resonator scheme has been adopted as schematically shown in Figure 31. The optical cavity is defined by a totally reflecting concave spherical mirror ( $ROC = 5$  m) and a 60% partially transmitting flat outcoupler. Five passages inside the YAG slab are accomplished by addition of two folding mirrors. Considering that the slab thickness is  $T = 4$  mm, a beam having 4 mm diameter provides optimal filling of the slab volume in 5 passages, and the Fresnel number of the cavity is  $N_f \sim 7$ . This resonator also has the advantage of allowing a fine tuning of the cavity-mode to gain-volume overlap by changing the folding mirrors angles and distances.

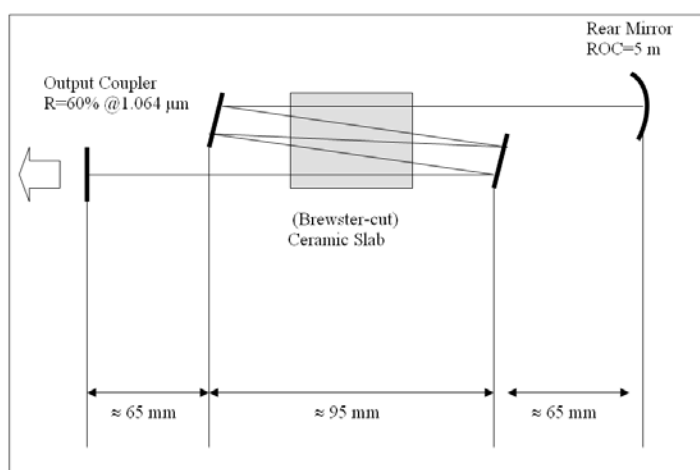


Figure 31. Multipass Folded Stable resonator(MFSR). Lateral direction (y) view.

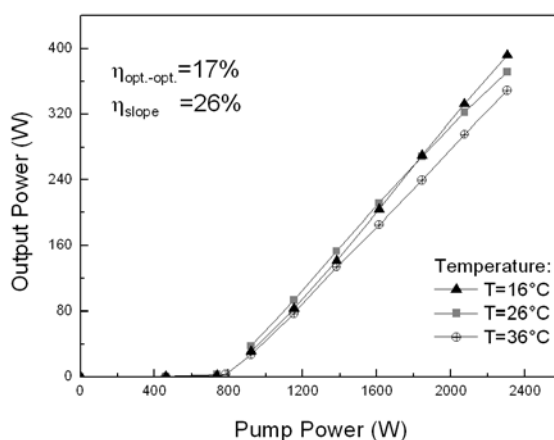


Figure 32. Extraction efficiency curves for the beam generated by the MFSR at different diode temperatures.

Typical power extraction curves are reported in Figure 32. Again these curves are obtained in a QCW regime both to avoid efficiency reductions due to the thermo-mechanical management and to allow testing with diode and slab passive cooling. Interestingly, given the large pump radiation absorption depth allowed by this architecture, the extraction efficiency results are substantially unaffected by large variations (20 °C) in the diode cooling temperature. Just to perform an efficiency comparison, laser action from the edge-pumped slab was also pursued with a simple two-mirror, 230 mm long resonator. The cavity consisted of a couple of flat mirrors, with 100% and 90% reflectivity. A maximum extracted power of 340 W was obtained, roughly 85% of the power obtained with the MFSR in the same pumping conditions, indicating a difficult attainment of an appropriate cavity mode with such an optical set-up. A reduction of the out-coupler reflectivity further caused a dramatic fall of the extraction efficiency.

Figure 33 shows the optical properties of the extracted beam. Beam diameter measurements along propagation have been performed as previously described [37], for both 10%-90% and 16%-84% intensity clipping levels. The obtained  $M^2$  values confirm the attainment of a smooth intensity distribution with Beam Parameter Products below (and actually close to) 3 mm.mrad making this scheme well suited for fiber delivered systems.

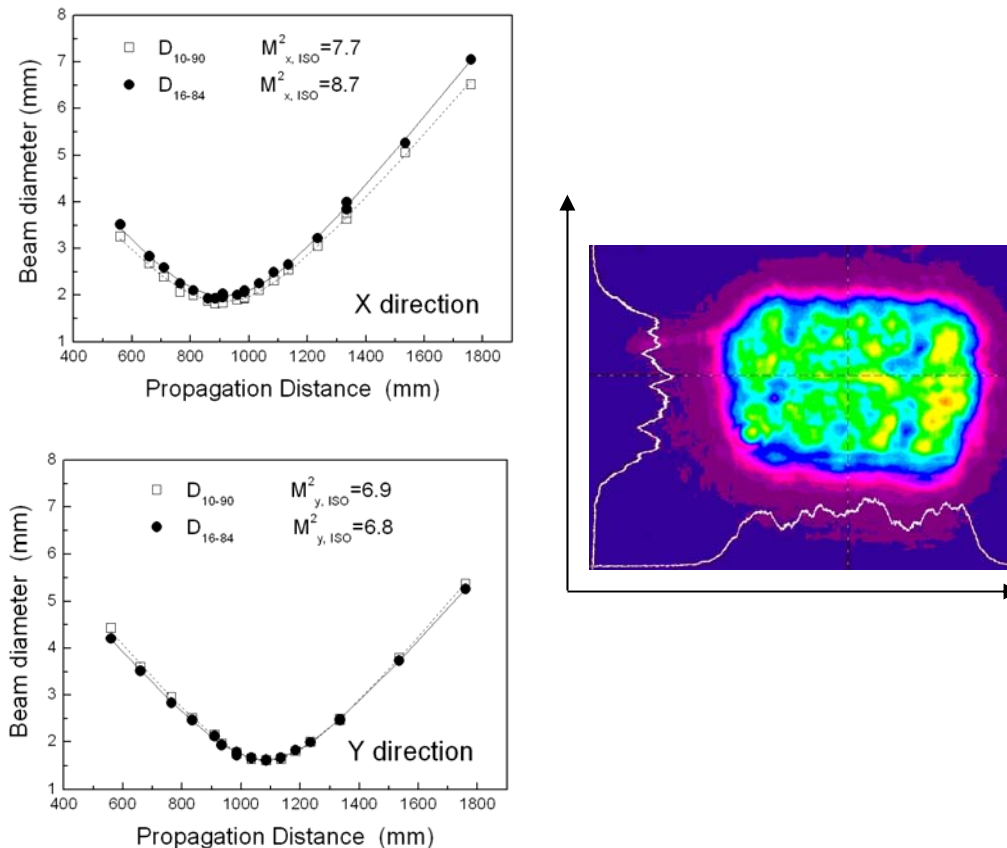


Figure 33. Propagation Caustics and Intensity Profiles for the beam extracted from the MFSR.

## Acknowledgments

The results presented in this chapter are the output of a long theoretical and experimental activity on thin ceramic Nd:YAG lasers with zig-zag internal propagation. This work enabled an assessment of the potential of this technology in the construction of medium to high power Diode Pumped Solid State Lasers (DPSSLs). The collaboration of a number of colleagues to this research activity is gratefully acknowledged (in alphabetic order: Maurizio De Rosa, Massimo D'Uva, Elena Favilla, Claudio Mingazzini, Mauro Pucci, Alessandra Rocco, Elisa Sani).

## References

- [1] G. Bonati, Prospects for the the Diode Laser Market: From science to conveyers. L.T.J. (2), pp.37-40, April 2010 ([www.laser-journal.de](http://www.laser-journal.de))
- [2] J. Caird, *Status of DPSSL Development*. Presented at "Fusion: Pathways to the Future", Washington, DC, September 27-28, 2006.
- [3] see for instance: [www.dilas.com](http://www.dilas.com)
- [4] see for instance: [www.ipgphotonics.com](http://www.ipgphotonics.com)
- [5] A. Giesen, H. Huegel, A. Voss, K. Wittig, U. Brauch, H. Opower, Scalable concept for diode-pumped high-power solid-state lasers. *Appl. Phys. B*, 58 (1994), 365-372.
- [6] M. Ciofini, A. Lapucci, Compact scalable diode pumped Nd:YAG ceramic slab laser. *Appl. Optics*, 43(33) (2004), 6174-6179.
- [7] E. Sani, E. Favilla, M. Ciofini, A. Lapucci, G. Bezzi, C. Mingazzini, S. Sangiorgi, Comparative Optical Characterization of Transparent Nd-doped YAG Ceramics and Single Crystals for Laser Applications. In *Advances in Science and Tecnology*, volume 45, pp. 2608-2613, *Trans Tech Publication Ltd.*, 2006.
- [8] K. Du, N. We, J. Xu, J. Giesekus, P. Loosen, R. Poprawe, Partially end-pumped Nd:YAG slab laser with a hybrid resonator. *Opt. Lett.*, 23(5) (1998), 370-372.
- [9] T. Kawashima et al., Diode-Pumped zig-zag slab laser for inertial fusion energy and applications. Paper MB19, *OSA/ASSP Conference, Santa Fe, New Mexico*, 1-4 February, 2004.
- [10] Daniel W. Trainor, Thinzag: a novel approach to solid state slab lasers. *Invited presentation, XVI GCL-HPL, Gmunden, Austria*, 4-8 September, 2006.
- [11] W. Koechner, *Solid State Laser Engineering*. 5<sup>th</sup> ed., Springer Verlag, Berlin, 1999.
- [12] R. Sheps, *Introduction to Laser Diode-Pumped Solid State Lasers*. SPIE Press, Tutorial Text in Optical Engineering, vol. TT53, 2001.
- [13] V. Reichler, K. W. Moerl, S. Unger, S. Jetschke, H.-R. Mueller, J. Kirchof, T. Sandrock, A. Harschack, A. Liem, J. Limpert, H. Zellmer, A. Tuennermann, Fiber-laser power scaling beyond the 1-kilowatt level by Nd:Yb co-doping. *SPIE Proc.*, 5777 (2005), 404-407.
- [14] E. S. Sherbakov, New achievements in development of superpower industrial fiber lasers and their applications. Paper TFII2-3-WED, *CLEO/Europe-EQEC 2005, Muenchen*, 12-17 June, 2005.

- [15] H. P. Chou, Y. L. Wang, V. Hasson, Compact and efficient DPSS Laser using diamond-cooled technology. *SPIE Proc.*, 5448 (2004), 550-560.
- [16] R. J. Shine, A. J. Alfrey, R. L. Byer, 40-W cw, TEM<sub>00</sub>-mode, diode-laser-pumped, Nd:YAG miniature-slab laser. *Opt. Lett.*, 20(5) (1995), 459-461.
- [17] Y. Liao, K. Du, S. Falter, J. Zhang, M. Quade, P. Loosen, and R. Poprawe, Highly efficient diode-stack, end-pumped Nd:YAG slab laser with symmetrized beam quality. *Appl. Opt.*, 36 (1997), 5872-5875.
- [18] A. Lapucci, M. Ciofini, Efficiency optimization for a diode pumped Nd:YAG ceramic slab laser. *Appl. Optics*, 44(20) (2005), 4388-4393.
- [19] A. Ikesue, T. Kinoshita, K. Kamata, and K. Yoshida, Fabrication and optical properties of high-performance polycrystalline Nd:YAG ceramics for solid-state lasers. *J. Am. Ceram. Soc.*, 78(4) (1995), 1033-1040.
- [20] J. Lu, M. Prabhu, K. Ueda, H. Yagi, T. Yanagitani, and A. Kudryashov, Highly efficient lasers using polycrystalline Nd:YAG ceramics. In XIII International Symposium on Gas Flow and Chemical Lasers and High-Power Laser Conference, A. Lapucci and M. Ciofini, eds., *Proc. SPIE*, 4184 (2001), 373-376.
- [21] J. Lu, K. Ueda, H. Yagi, T. Yanagitani, Y. Akiyama, and A. A. Kamiskii, Neodymium doped yttrium aluminum garnet (Y<sub>3</sub>Al<sub>5</sub>O<sub>12</sub>) nanocrystalline ceramics – a new generation of solid state laser and optical materials. *J. Alloys Compd.*, 341 (2002), 220-225.
- [22] [www.konoshima.co.jp](http://www.konoshima.co.jp).
- [23] [www.vloc.com](http://www.vloc.com).
- [24] I. Shoji, S. Kurimura, Y. Sato, and T. Taira, Optical properties and laser characteristics of highly Nd<sup>3+</sup>-doped Y<sub>3</sub>Al<sub>5</sub>O<sub>12</sub> ceramics. *Appl. Phys. Lett.*, 77(7) (2000), 939-941.
- [25] [www.jenoptik.com](http://www.jenoptik.com)
- [26] M. Ciofini, E. Favilla, A. Lapucci, E. Sani, A. Capanni, and L. Tommasi, MILD: a laser altimeter transmitter for a Mercury planetary orbiter. *Appl. Phys. B*, 92 (2008), 431-438.
- [27] J. M. Eggleston, T. J. Kane, K. Kuhn, J. Unternahrer, and R. L. Byer, The slab geometry Laser – Part I: Theory. *IEEE J. Quantum Electron.*, QE-20 (1984), 289-301.
- [28] D. Bigazzi, P. Mazzinghi, and M. Vannini, Thermal effects in flashlamp pumped solid state lasers”, in “Sorgenti laser a stato solido e tecnologie associate. G. C. Righini ed., collana Quaderni di Ottica e Fotonica, Centro Editoriale Toscano, Pontassieve – Firenze – Italy, 1996, 41-54.
- [29] A. Lapucci, M. Ciofini, E. Favilla, E. Sani, M. De Rosa, G. Mincuzzi, and A. Rocco, Quantitative analysis of the thermal distortions in a 100 W CW Nd:YAG ceramic slab laser. *J. Europ. Opt. Soc. Rapid Publ.*, 2 (2007), 07020.
- [30] A. Lapucci, M. Ciofini, M. De Rosa, E. Favilla, E. Sani, A. Rocco, Experimental study of face- and edge- pumped ceramic slab DPSSLs in the 100-500 W power range. *Spie Proc.*, 7131 (2008), 713114-713121, (2008).
- [31] [www.lasertel.com](http://www.lasertel.com)
- [32] [www.lambdares.com](http://www.lambdares.com)
- [33] A.E. Siegman, *Lasers*. University Science Books, Mill Valley Calif. 1986, Chap. 22.
- [34] A. Lapucci, A. Labate, F. Rossetti, and S. Mascalchi, Hybrid stable-unstable resonators for diffusion-cooled CO<sub>2</sub> slab lasers. *Appl. Opt.*, 35 (1996), 3185-3192.

- 
- [35] M. Ciofini, E. Favilla, A. Lapucci, and E. Sani, Propagation parameters of the beam extracted from a diode pumped Nd:YAG ceramic slab laser with a hybrid stable-unstable resonator. *Opt. and Laser Tech.*, 39 (2007), 1380-1388.
- [36] A. Lapucci and M. Ciofini, Parametric study of a Hybrid Stable Unstable Resonator (HSUR) for slab lasers in strongly non-confocal configuration. *SPIE Proc.*, 7751 (2010).
- [37] ISO standard 11146-1 *Lasers and laser-related equipment – Test methods for laser beam widths, divergence angle and beam propagation factor- Part 1: stigmatic and simple astigmatic beams* and 11146-3 *Lasers and laser-related equipment – Test methods for laser beam widths, divergence angle and beam propagation factor - Part 3: Alternative test methods and geometrical laser beam classification and propagation*.
- [38] B. V. Hunter, K. H. Leong, C. B. Miller, J. F. Golden, R. D. Glesias, P. J. Lavery, Selecting a high-power fiber optic laser beam delivery system. *Proceedings ICALEO*, Laser Institute of America, 81E (1996), 173-182.

Reproduced with permission of the copyright owner. Further reproduction prohibited without permission.